Hindawi
International Journal of Energy Research
Volume 2024, Article ID 7724598, 15 pages
https://doi.org/10.1155/2024/7724598

Research Article

Synthesis of Stable and Efficient Electrocatalysts for Hydrogen Evolution: Hierarchical NiMo-Based Hollow Nanotubes

Bal Sydulu Singu, Debasish Mandal, Jae Eun Sim, and Hansung Kim

Electrochemical Energy Laboratory, Department of Chemical and Biomolecular Engineering, Yonsei University, Seoul 03722, Republic of Korea

Correspondence should be addressed to Hansung Kim; elchem@yonsei.ac.kr

Received 15 November 2023; Revised 24 January 2024; Accepted 22 April 2024; Published 11 May 2024

Academic Editor: Samuel Lalthazuala Rokhum

Large-scale development of low-cost, efficient, and stable powder electrocatalysts for the hydrogen evolution reaction (HER) in alkaline solutions is a key step toward commercial hydrogen production. Herein, a hierarchical NiMo-MoO_{3-x} hollow nanotube (NiMo-MoO_{3-x}-HNT) with bifunctional groups as an efficient HER electrocatalyst was strategically invented using an MoO_3 nanorod (MoO_3–NR) as the precursor. The synthesis mechanism of the NiMo-MoO_{3-x}-HNT is established based on in-depth investigations using diffraction, spectral, and microscopy results. Experimental results suggest that the NiMo-MoO_{3-x}-HNT exhibits excellent electrocatalytic HER performance in 1 M KOH, with a low overpotential of 26.5 mV@10.0 mA cm^{-2} and a small Tafel slope of 32.6 mV dec^{-1}. These values are comparable to those of cutting-edge electrocatalysts based on platinum-group metals. Moreover, it exhibits an almost unaffected cyclic stability over 50,000 cycles and robust durability over 98 h. This remarkable performance is attributed to its bifunctional groups and the porous hierarchical hollow nanotubular morphology. In summary, this study proposes a novel, efficient, and cost-effective strategy for the development of noble metal-free, high-performance HER electrocatalysts.

1. Introduction

Hydrogen is considered a future energy carrier that can replace traditional fossil fuels [1, 2]. To meet global demands, electrochemical water splitting is considered the most efficient method for the production of clean hydrogen [3–6]. In the industry, hydrogen is produced by water electrolysis in an alkaline medium because of its ecofriendliness and economic viability [7]. For water splitting in an alkaline solution, platinum group metals (PGMs: Pt and Ru), especially Pt, are highly efficient electrocatalysts for hydrogen evolution reaction (HER) with very low overpotential; however, their high cost and scarcity restrict their large-scale application [8]. An ideal HER electrocatalyst should have low overpotential and long durability, and its bulk production should be economically feasible. Consequently, the development of an efficient earth-abundant HER electrocatalyst in an alkaline solution is crucial for replacing PGM-based catalysts in large-scale applications [9, 10].

Tremendous efforts have been made on non-PGMs (including Ni, Co, Mo, and Fe) and their compounds, such as alloys and oxides, for use as potent water-splitting catalysts [11–17]. After Pt/C, alloys such as PtCo, RuCo, RuNi, and NiMo are among the most promising candidates for HER [5, 18–20]. Alloys have been shown to enhance HER catalytic activity by fine-tuning the binding energy of hydrogen on the catalyst surface [21]. In particular, the NiMo alloy has exhibited immense potential as an alkaline HER electrocatalyst because of its cost-effectiveness and unique properties. NiMo has an electronic surface state similar to that of platinum [11–13] and induces a synergistic effect through electron transfer from electron-rich Ni to electron-deficient Mo [22]. Several approaches have been suggested for the design of the NiMo alloy-based HER electrocatalysts in pow-

der form, and overpotential ≥ 65 mV and Tafel slope ≥ 36.6 mV dec^{-1} have been achieved [3, 5, 11, 23, 24]. Therefore, the development of a high-performance powder electrocatalyst based on NiMo alloy is one of the potential candidates to substitute Pt/C.

The performance of the NiMo alloy can be improved using several approaches, such as tuning the electronic structure/chemical composition and synthesizing well-organized porous morphologies. Typically, two critical reactions occur on the catalyst surface during molecular H_2 production from water: cleavage of the H–OH bond to its intermediates and conversion of the intermediates to H_2. Several studies have demonstrated that metal oxides are effective in cleaving the H–OH bond, whereas metals with optimal M-H_{ad} energies play a crucial role in converting the intermediates to H_2 [25]. Therefore, metal-metal oxide heterostructures can accelerate the overall HER performance. Recently, some metal-metal oxide-based heterostructures (Pt-Ni$(OH)_2$, Ru-O-Mo, and MoNi-Ni$(OH)_2$) have been reported to demonstrate bifunctional effects in improving the catalytic behavior of HER [26–29]. Further, the intrinsic activity of electrocatalysts can be tuned using several approaches, including tuning electronic conductivity, controlling the dimensions of nanostructured materials (0 to 3 D), and creating porous/hollow/hierarchical structures [14, 15, 30–33]. Typical hierarchical hollow nanotubular structured materials represent a novel class of materials with unique structural dimensions [16, 17, 34–38]. The 1D core hollow nanotube (HNT) provides an easier charge-transport network with reduced scattering, facilitates rapid mass transport, and maintains electrolyte accessibility through its hollow tunnel [39], whereas the hierarchical 2D surface provides a large effective catalytic surface area, which prevents particle aggregation and accelerates the release of H_2 bubbles [40]. Thus, electrocatalysts featuring hierarchical hollow nanotube structures with metal-metal oxide heterostructures can demonstrate excellent HER performance.

Motivated by this concept, a porous hierarchical NiMo-MoO_{3-x}-HNT electrocatalyst with bifunctional groups (NiMo alloy and MoO_{3-x} oxide) was developed for the HER. The hollow nanotube with a hierarchical 2D surface, consisting of metal-metal oxide, was prepared through a hydrothermal process followed by a thermal reduction process utilizing MoO_3 nanorods as a one-dimensional template to induce Kirkendall voids. To optimize the synthesis process of NiMo-MoO_{3-x}-HNT, the electrocatalysts and intermediate products were characterized using various techniques, including diffraction, spectroscopy, and microscopy. The electrocatalytic HER performance of the catalysts was investigated in a 1 M KOH solution using various electrochemical techniques. The prepared catalyst exhibited favorable attributes, including a high surface area, porosity, and effective synergy between NiMo alloy and MoO_{3-x} components, making it a promising candidate for electrocatalytic applications, particularly in the context of HER. Furthermore, a study on the catalyst's durability after a cycle life test was conducted, and its electrochemical activity, morphological changes, and chemical states were analyzed.

2. Experimental Section

2.1. Materials. Ammonium heptamolybdate (Sigma-Aldrich, purity 99.0%), nickel acetate tetrahydrate (purity 99.98%, Sigma-Aldrich), potassium hydroxide (Sigma-Aldrich, purity ≥ 85%), nitric acid (purity 64–66%, Duksan Reagents), and Pt/C (Johnson-Matthey, 40 wt%) were used as-received.

2.2. Synthesis of MoO_3 Nanorod. Ammonium heptamolybdate (1.0 g) was dissolved in 33.4 mL of deionized water. After complete dissolution, 6.6 mL of HNO_3 was added dropwise to this solution under constant stirring. The solution was transferred to a Teflon-lined autoclave (50 mL) and hydrothermally treated at 180°C for 20 h in an electric oven [41]. The reactor was allowed to cool naturally to room temperature after the completion of the reaction. The resulting MoO_3 nanorod (MoO_3-NR) was filtered, washed with water and ethanol, and dried overnight at 60°C.

2.3. Synthesis of Hierarchical $NiMoO_4$-Ni$(OH)_2$ Hollow Nanotube. In this study, MoO_3-NR (0.1 g) was dispersed in 20 mL of deionized water and sonicated for a few minutes, after which it remained dispersed for a long time. Subsequently, nickel acetate (0.99 gm, 0.1 M) was added to the MoO_3-NR dispersion, which resulted in instant precipitation. The precipitate was sonicated and stirred for a few minutes. Next, 20 mL of ethanol was added, and the solution was stirred for another 15 min. Thereafter, the solution was transferred to a Teflon-lined autoclave and heat-treated in an electric oven for 5 h at 90°C. The reactor was allowed to cool naturally to room temperature after the completion of the reaction. The product, designated as $NiMoO_4$-Ni$(OH)_2$ hollow nanotube ($NiMoO_4$-Ni$(OH)_2$-HNT), was collected by filtration and was washed with water and ethanol before drying overnight at 60°C.

2.4. Synthesis of Hierarchical NiMo-MoO_{3-x} Hollow Nanotube. The targeted hierarchical NiMo-MoO_{3-x} hollow nanotube (NiMo-MoO_{3-x}-HNT) catalyst was prepared by thermal reduction of the $NiMoO_4$-Ni$(OH)_2$-HNT (0.2 g) at 500°C in a tube furnace for 2 h at a heating rate of 10°C/min in an Ar/H_2 (90/10, V/V) atmosphere. The influence of the reduction temperature was also explored through the synthesis of catalysts at different temperatures, spanning from 400 to 800°C. The prepared electrocatalysts were designated as Ni-Mo–x, where x indicated the reduction temperature.

3. Structural Characterization

Powder crystallographic patterns of the specimens were obtained using a Rigaku MiniFlex X-ray diffractometer with CuK radiation in the scan range of 10–80° (2θ). Their powder morphology images were captured using a field-emission scanning electron microscope (FE-SEM, JEOL-7800F). JEM-F200 was used to capture transmission electron microscopy (TEM) images and perform electrochemical dispersive spectroscopy (EDS). The mass percentages of the elements in the specimens were determined using inductively coupled plasma optical emission spectrometry (ICP-OES, Thermo Scientific iCAP-6000) by dissolving the specimens in an

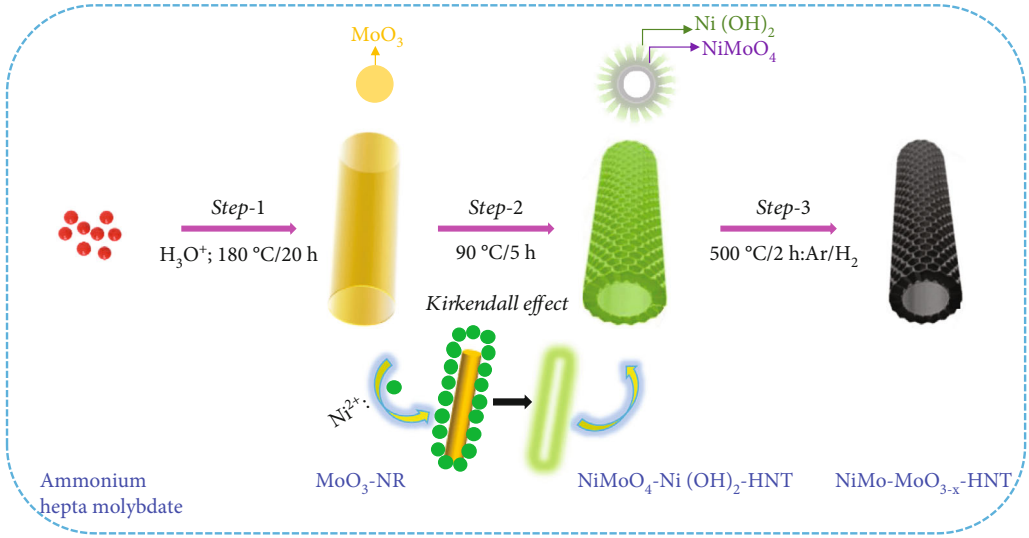

FIGURE 1: Graphical presentation of the synthesis of hierarchical NiMo-MoO_{3-x} hollow nanotube.

acid. Surface area and pore size distribution curves were acquired using an Autosorb-iQ 2ST/MP system (Quantachrome Instruments). The chemical states of the specimens were analyzed by X-ray photoelectron spectroscopy (XPS, K-alpha, Thermo VG).

4. Electrochemical Measurements

All the electrochemical measurements were performed using a Biologic VSP electrochemical workstation with a standard three-electrode system. The catalyst ink was formulated by subjecting 10 mg of the catalyst, 1 mL of isopropanol, and 75 μL of Nafion to sonication for 1 hour. Once a uniform catalyst ink was achieved, 50 μL of this ink was applied via drop-coating onto a rotating ring disk electrode (RRDE) measuring 5.6 mm in diameter and possessing a surface area of 0.247 cm^2. The electrochemical HER performance of the catalyst was determined using the catalyst-loaded RRDE as the working electrode, Hg/HgO as the reference electrode, and a graphite rod as the counter electrode, all immersed in a 1 M KOH solution. To convert the potential scale to a reversible hydrogen electrode (RHE), an adjustment of 0.922 V was made. This value was determined through the calibration of the Hg/HgO electrode by introducing H_2 gas into a 1 M KOH solution, with two Pt wires serving as the counter and working electrodes separately. The catalyst was activated through the five cycles of cyclic voltammetry (CV) at a scan rate of 1 mV s^{-1}, covering a potential range from 0.1 to −0.5 V versus the RHE. All linear sweep voltammetry (LSV) profiles were captured at a rotation speed of 2500 rpm and a scan rate of 5 mV s^{-1}. Catalyst stability was evaluated using CV at a sweep rate of 200 mV s^{-1} over a potential range of 0.2 to −0.25 V versus RHE for 50,000 cycles. Further, the durability of the optimized catalyst was investigated using the chronopotentiometric (CP) method at a current density of 10 mA cm^{-2} for 98 h. The IR correction for all LSV curves was performed by calculating E_{IR} (E_{IR}-corrected potential) using the formula $E_{IR} = E_M - I \times R_S$, where E_M represents the measured potential and R_S is the electrode resistance determined through electrochemical impedance spectroscopy in 1 M KOH.

5. Results and Discussion

5.1. Synthesis and Characterization. The synthesis method for NiMo-MoO_{3-x}-HNT is described graphically in Figure 1. In the first step, MoO_3-NR was synthesized hydrothermally. In the second step, the MoO_3-NR was modified to $NiMoO_4$-$Ni(OH)_2$-HNT using a hydrothermal method. Finally, the optimized catalyst NiMo-MoO_{3-x}-HNT was synthesized by the thermal reduction of $NiMoO_4$-$Ni(OH)_2$-HNT in an Ar/H_2 atmosphere at 500°C. The reaction mechanism for the synthesis of NiMo-MoO_{3-x}-HNT from MoO_3-NR was deduced by in-depth probing of the diffraction, spectral, and microscopic results, which are discussed in detail. In step 1, ammonium heptamolybdate was converted into MoO_3-NR by hydrothermal treatment [42]. The nanorod structure of MoO_3-NR, characterized by a high aspect ratio, was facilitated by the predominant growth of MoO_3 crystals along the [001] plane in a highly acidic medium [41]. In step 2, Ni^{2+} ions from $Ni(CH_3COO)_2$ were physically adsorbed onto the MoO_3-NR surface. This phenomenon was substantiated by EDAX mapping, which indicated the presence of adhered Ni^{2+} ions on the MoO_3-NR surface (Figure S1 and Eq. (1)). Consequently, the unbalanced CH_3COO^- ions reacted with H_2O, resulting in the generation of OH^- ions, as represented by Eq. (2). Subsequently, under hydrothermal conditions at 90°C, a portion of the generated OH^- ions reacted with the Ni^{2+} ions present in MoO_3-Ni^{2+} (according to Eq. (1)), culminating in the formation of a hierarchical nanosheet structure composed of $Ni(OH)_2$. This process occurred on the surface of MoO_3-NR, as illustrated by Eq. (3). The hierarchical nanosheet structure growth of $Ni(OH)_2$ proceeded through the following steps: (i) nucleation of $Ni(OH)_2$ on the MoO_3 surface; (ii) nucleation aggregation

and nanocrystal formation under the driving forces of high surface energy and electrostatic interactions; (iii) anisotropic growth of the $Ni(OH)_2$ crystal along the [001] plane because of the lower energy barrier, leading to the formation of hierarchical $Ni(OH)_2$ nanosheets; and (iv) further development of $Ni(OH)_2$ nanosheets by the Ostwald ripening process, during which unstable smaller $Ni(OH)_2$ particles were dissolved and attached to the $Ni(OH)_2$ nanosheets connected to the MoO_3 surfaces [40, 43]. The MoO_3-NR was transformed into a hollow nanotube through a chemical etching process involving OH^- and MoO_3-NR. This reaction led to the creation of MoO_4^{2-} ions (as shown in Eq. (4)), a phenomenon further facilitated by the heightened water solubility of MoO_3 at elevated temperatures. Consequently, Kirkendall voids were formed (as depicted in Figure 2) [44]. The resulting MoO_4^{2-} ions were balanced by reacting with Ni^{2+} ions, yielding $NiMoO_4$ in chemical transformation outlined in Eq. (5). Simultaneously, a portion of the generated $Ni(OH)_2$ on the MoO_3 surface reacted with MoO_3, ultimately producing $NiMoO_4$ (as in Eq. (6)). This particular chemical reaction may also have a role in the formation of Kirkendall voids.

$$MoO_3 + Ni^{2+} \longrightarrow MoO_3 - Ni^{2+} \quad (1)$$

$$CH_3COO^- + H_2O \longrightarrow CH_3COOH + OH^- \quad (2)$$

$$Ni^{2+} + 2OH^- \longrightarrow Ni(OH)_2 \quad (3)$$

$$MoO_3 + 2OH^- \longrightarrow MoO_4^{2-} + H_2O \quad (4)$$

$$MoO_4^{2-} + Ni^{2+} \longrightarrow NiMoO_4 \quad (5)$$

$$MoO_3 + Ni(OH)_2 \longrightarrow NiMoO_4 + H_2O \quad (6)$$

Finally, in step 3, when the $NiMoO_4$-$Ni(OH)_2$-HNT was annealed at 500°C under a reduction atmosphere (Ar/H_2), it was converted to a hierarchical NiMo-MoO_{3-x} hollow nanotube through the elimination of the maximum possible amount of oxygen and water.

The morphologies of the prepared samples were investigated using FE-SEM and TEM. The MoO_3-NR exhibited a solid nanorod-like morphology, with a diameter and length of approximately 200 nm and 5–10 μm, respectively, as confirmed by FE-SEM (Figure 2(a)) and TEM images (Figure 2(b)). Furthermore, the selected area electron diffraction (SAED) pattern of the MoO_3-NR (inset of Figure 2(b)) revealed ordered lines, indicating its single-crystalline nature. Figures 2(c)–2(e) provide valuable insights into how the growth process of $NiMoO_4$-$Ni(OH)_2$-HNT is influenced by the reaction time. As the hydrothermal reaction time was increased from 0.5 h to 5 h in step 2, the MoO_3-NR core gradually decreased and eventually disappeared after 5 h. As the reaction time progressed, the MoO_3 core underwent a comprehensive conversion into $NiMoO_4$ and/or experienced erosion through etching, facilitated by its heightened water solubility at elevated temperatures. Concurrently, the thickness of $Ni(OH)_2$ on the MoO_3-NR surface increased proportionally with reaction time, as evidenced by the X-ray diffraction (XRD) analysis and detailed in subsequent sections. Collectively, these factors led to the emergence of well-defined hollow nanotubes, contributing to the formation of the $NiMoO_4$-$Ni(OH)_2$-HNT structures, as illustrated in Figure 2(g). A reaction time of 5 h was required to consistently generate uniform nanotubular structures. The FE-SEM (Figure 2(e)) and TEM (Figure 2(f)) images of the $NiMoO_4$-$Ni(OH)_2$-HNT exhibited a hollow nanotube morphology with a shell composed of hierarchical 2D nanosheets. The SAED pattern (inset of Figure 2(f)) of the nanosheets present in the shell showed two diffraction rings, identified as the (100) and (110) planes of $Ni(OH)_2$. The diameter and length of the $NiMoO_4$-$Ni(OH)_2$-HNT were in the ranges of approximately 200–500 nm and 1–5 μm, respectively. The shorter length of the $NiMoO_4$-$Ni(OH)_2$-HNT compared with that of the MoO_3-NR precursor may be attributed to the etching/solubility of the MoO_3-NR at elevated temperatures.

The FE-SEM (Figure 3(a)) and TEM (Figure 3(b)) images of the targeted NiMo-MoO_{3-x}-HNT indicated that its morphology was identical to that of the precursor. Thus, the hollow nanotube structure of the catalyst consists of hierarchical 2D nanosheets, which provide a large effective catalytic surface area for the HER. The SAED pattern of the NiMo-MoO_{3-x}-HNT (Figure 3(c)) exhibited four diffraction rings, identified as the (331), (051), (171), and (282) planes of the NiMo alloy. The EDAX mapping images of the NiMo-MoO_{3-x}-HNT (Figure S2) indicate that Ni, Mo, and O are uniformly distributed throughout the HNT. The presence of O in the NiMo-MoO_{3-x}-HNT may be attributed to the presence of the MoO_{3-x} functional group of the catalyst and the formation of a thin oxide layer on the alloy surface owing to the sensitivity of the alloy to air. The MoO_{3-x} in the NiMo-MoO_3-HNT exists in an amorphous state, as indicated by blue circles in the HR-TEM image (Figure 3(d)). The area outside the blue circle represents the NiMo-distinctive alloy characteristics, as indicated by the d-spacing (0.19, 0.20, 0.21, and 0.22 nm) fringes (Figure 3(d)), confirming the development of bifunctional groups in the NiMo-MoO_{3-x}-HNT catalyst. The structural changes in the catalysts synthesized at various reducing temperatures in step 3 were investigated using FE-SEM (Figure S3). When the annealing temperature was increased to 600°C, the morphological integrity of the prepared alloys started to agglomerate, and the size was reduced because of the thermal reduction process. Above 700°C, the morphological integrity of the prepared alloys was destroyed, and they were compressed to a denser state, where there were no hierarchical nanosheet units were present. Therefore, in order to maintain the shape of the nanotube, it is necessary to maintain the thermal reduction temperature below 500°C.

Crystal structures of the prepared materials were investigated using XRD and are presented in Figure 4. The diffraction pattern of the MoO_3-NR, as shown in Figure 4(a) (A), perfectly matched with the crystal peaks of α-MoO_3 (JCPDS no. 35-0609). The diffraction pattern of the $NiMoO_4$-$Ni(OH)_2$-HNT (Figure 4(a)) (B) consisted of $NiMoO_4$ (JCPDS no. 13-0128) and $Ni(OH)_2$ (JCPDS no. 01-1047) crystal peaks, indicating the formation of a $NiMoO_4$-

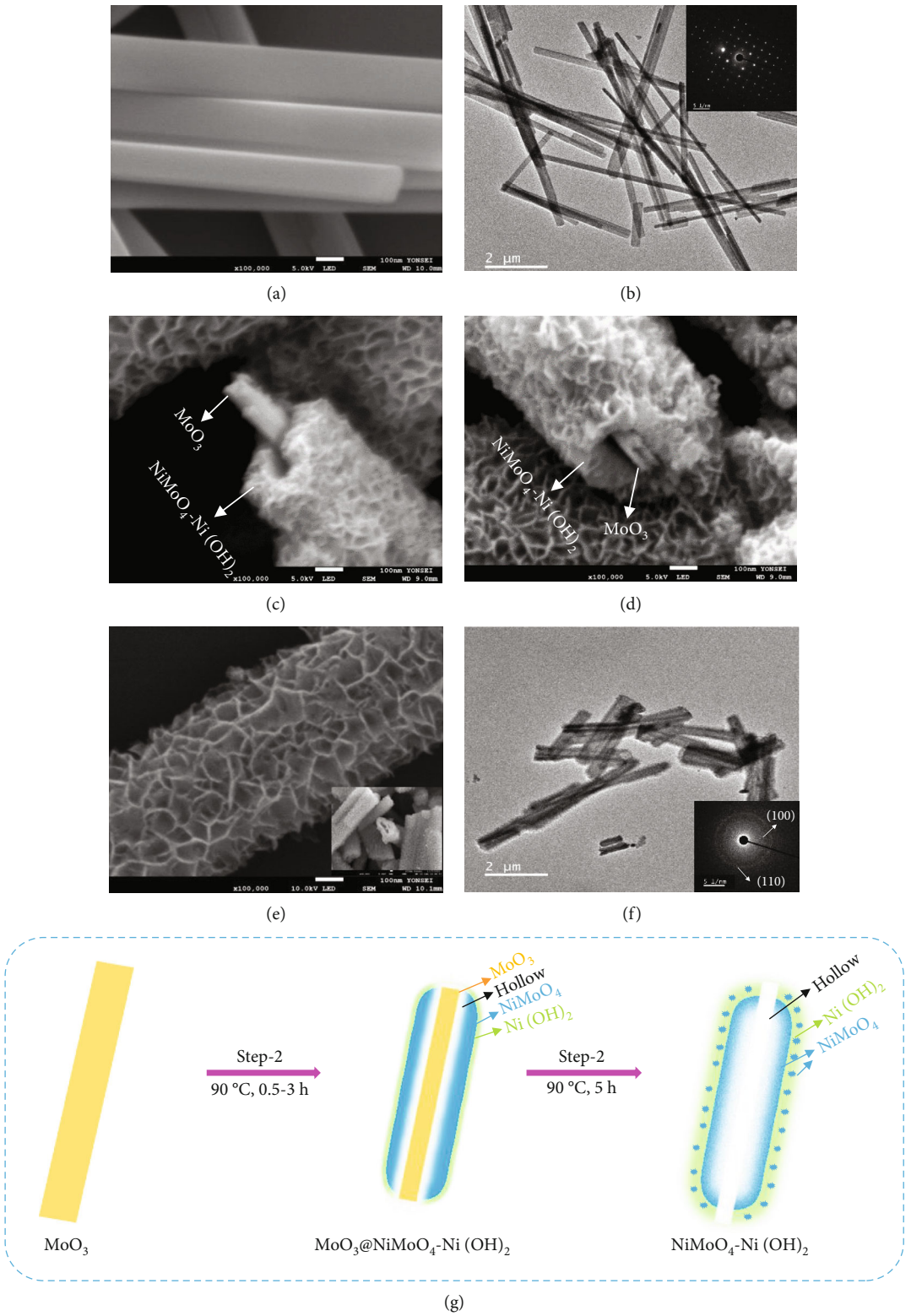

Figure 2: (a) FE-SEM and (b) TEM and SAED pattern (inset) of MoO_3-NR. FE-SEM images of $NiMoO_4$-$Ni(OH)_2$-HNT prepared at 90°C for different reaction time intervals: (c) 0.5 h, (d) 3 h, and (e) 5 h. (f) TEM image and SAED pattern (inset) of $NiMoO_4$-$Ni(OH)_2$-HNT and (g) graphical image illustrating the growth of $NiMoO_4$-$Ni(OH)_2$-HNT.

$Ni(OH)_2$-HNT structure. The $Ni(OH)_2$ crystal peaks were predominant because they were present on the outer surface of the $NiMoO_4$-$Ni(OH)_2$-HNT. Furthermore, the hydrothermal reaction time-dependent crystal growth of the $NiMoO_4$-$Ni(OH)_2$-HNT was investigated by measuring the XRD patterns at different time intervals, as shown in

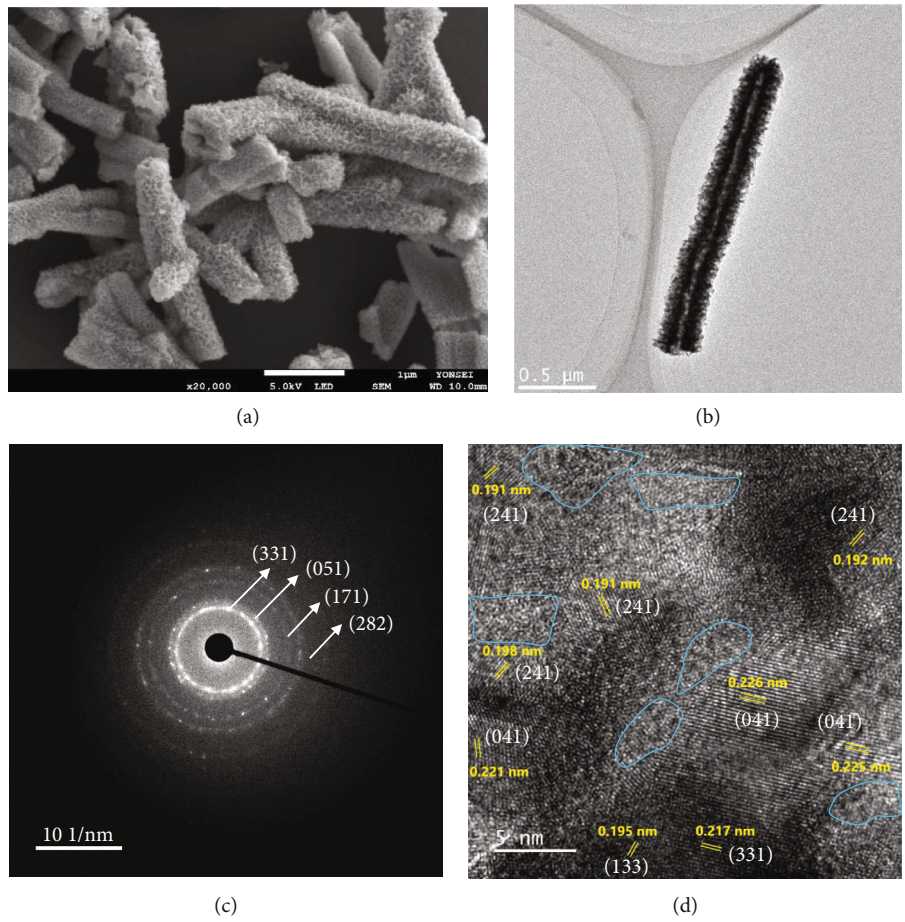

Figure 3: (a) FE-SEM, (b) TEM, (c) SAED pattern, and (d) HR-TEM images of NiMo-MoO_{3-x}-HNT.

Figure S4. When the hydrothermal reaction time at step 2 was increased from 0.5 h to 10 h (step 2), the peak of MoO_3 steadily decreased and disappeared, whereas the peak of $Ni(OH)_2$ strengthened and $NiMoO_4$ appeared. This coincides with the result depicted in Figure 2, which shows that as the hydrothermal reaction progresses, MoO_3 disappears, creating a void in the nanotube, and the thickness of $Ni(OH)_2$ gradually increases on the surface. The diffraction pattern of the targeted NiMo-MoO_{3-x}-HNT (Ni-Mo-500) catalyst (Figure 4(a)) (C) comprised a mixture of the Ni fcc phase (JCPDS no. 70-0989) with a slight shift and the NiMo-phase (JCPDS no. 48-1745), which was consistent with the previously reported Ni_2Mo-alloy pattern [45]. The XRD patterns of the catalysts synthesized at various reducing temperatures (400–800°C) at step 3 are shown in Figure 4(b). The XRD pattern of the Ni-Mo-400 catalyst was almost identical to that of the Ni-Mo-500 catalyst, although the crystal peaks of Ni-Mo-500 were positively shifted by 0.32° in comparison with those of Ni-Mo-400, possibly because of the effective synergy between Ni and Mo in Ni-Mo-500. For the Ni-Mo-600 catalyst, a new XRD peak appeared at $2\theta = 40.4°$ for the (110) plane of Mo (JCPDS no. 01-1207), and its crystal peaks were negatively shifted by 1.07° relative to the Ni-Mo-500 peaks. This result indicated that the Mo metal was slightly separated from the alloy, thereby weakening the synergy between Ni and Mo. When the temperature was increased from 600°C to 700 and 800°C, the XRD patterns comprised a mixture of prominent Mo-metal and Ni_3Mo-alloy (JCPDS no. 65-5305) phases. This finding indicates that at higher temperatures, the catalyst decomposes into Ni_3Mo-alloy and Mo-metal. Consequently, the XRD analysis suggests that Ni-Mo-500 has the highest synergy between Ni and Mo.

The compositions and electronic structures of the prepared catalysts and their precursors were investigated using XPS, as shown in Figure 5 and Figure S5, respectively. The Ni-2p core-level spectrum of the $NiMoO_4$-$Ni(OH)_2$-HNT (Figure 5(a)) exhibited Ni^{2+}-$2p_{3/2}$ and Ni^{2+}-$2p_{1/2}$ peaks at binding energies (BE) of approximately 855.9 and 873.5 eV, respectively, with a separation of 17.7 eV [46]. As evidenced in Figure 5(b), the NiMo-MoO_{3-x}-HNT electrocatalyst exhibited two main peaks at 852.8 and 870.0 eV, corresponding to the Ni^0-$2p_{3/2}$ and Ni^0-$2p_{1/2}$ electrons, revealing the almost complete transition of the Ni^{2+} state into the metallic Ni^0 state. The higher binding energy of Ni^0-$2p_{3/2}$ in the NiMo-MoO_{3-x}-HNT electrocatalyst compared with that of the pure Ni metal (the binding energy of Ni^0-$2p_{3/2}$ in pure Ni metal is 852.6 eV) demonstrated the existence of the alloy state [47]. The presence of small humps at BEs of approximately 855.9 and 873.5 eV in the NiMo-MoO_{3-x}-HNT electrocatalyst

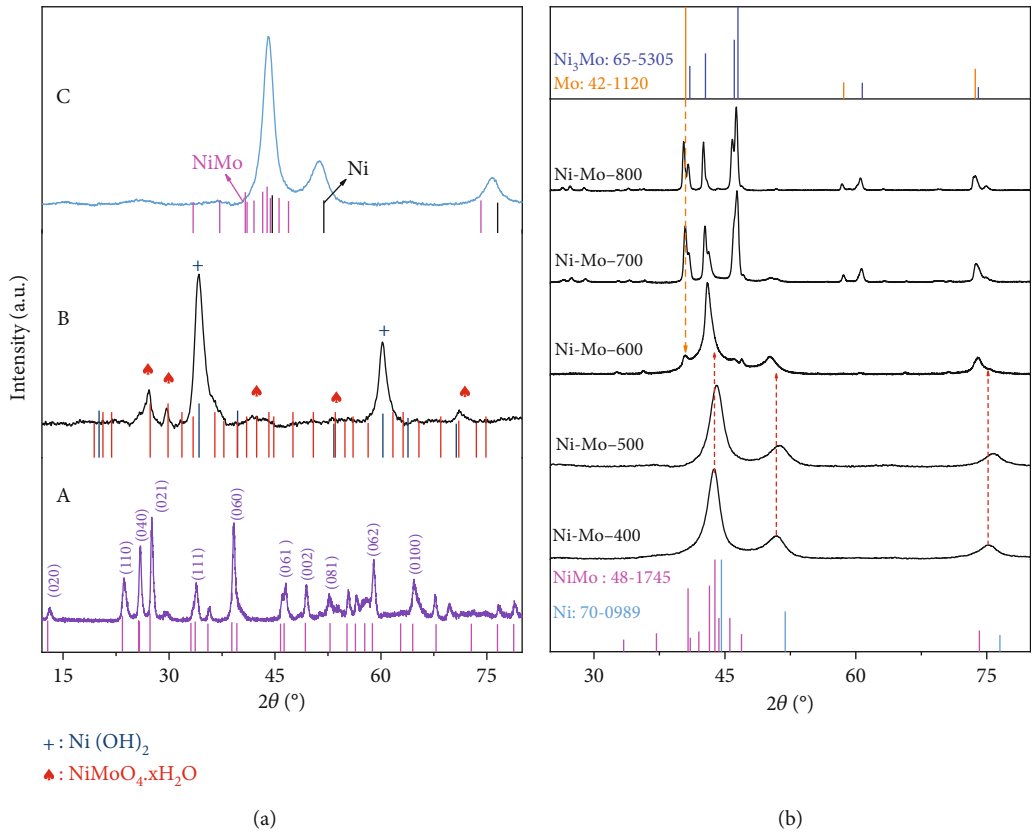

FIGURE 4: (a) XRD patterns of (A) MoO_3-NR, (B) $NiMoO_4$-$Ni(OH)_2$-HNT, and (C) NiMo-MoO_{3-x}-HNT. (b) XRD patterns of catalysts prepared at different reduction temperatures.

(Figure 5(b)), corresponding to the Ni^{2+}-$2p_{3/2}$ and Ni^{2+}-$2p_{1/2}$ electrons, may be explained by surface oxidation in the presence of air [48].

For the Mo-3*d* analysis, a significantly lower Mo-3*d* binding energy shift in the $NiMoO_4$-$Ni(OH)_2$-HNT (Mo^{6+}-$3d_{5/2}$ with BE of 232.34 eV) compared with that in the MoO_3-NR (Mo^{6+}-$3d_{5/2}$ with BE of 233.1 eV) precursor (Figure 5(d)) indicated the successful transformation of MoO_3 into $NiMoO_4$. The deconvoluted Mo-3*d* XPS peak of the NiMo-MoO_{3-x}-HNT (Figure 5(e)) revealed eight distinct peaks. Among these, two peaks corresponded to the metallic Mo^0 state, whereas the remaining six peaks indicated various oxide states (Mo^{4+}, Mo^{5+}, and Mo^{6+}: MoO_{3-x}, where $0 < x < 1$) [5]. Surprisingly, despite the electron transfer from Ni to Mo in the Ni-Mo-500 electrocatalyst, a positive shift was observed in the BE of the Mo^0 state (228.17 eV) compared with that of the pure Mo metal (227.85 eV). This finding suggests electron transfer from Mo^0 to MoO_{3-x}, implying the presence of a NiMo-MoO_{3-x} bifunctional structure with synergy between the NiMo alloy and MoO_{3-x}. Furthermore, within the NiMo-MoO_{3-x}-HNT, the Mo^{6+} state displayed a notably reduced BE of 231.91 eV, in contrast to the MoO_3-NR (233.1 eV) as well as the $NiMoO_4$-$Ni(OH)_2$-HNT (232.34 eV). Similarly, the state in the NiMo-MoO_{3-x}-HNT exhibited a lower binding energy (Mo^{4+}-$3d_{5/2}$ with a BE of 229.24 eV) compared with that of the pure MoO_2 (Mo^{4+}-$3d_{5/2}$ with a BE of 229.9 eV). These observations suggest an electron transport mechanism from Ni^0 to Mo^0 and subsequently from Mo^0 to molybdenum oxide. In essence, the NiMo-MoO_{3-x}-HNT predominantly consists of Ni^0 and Mo^0 metallic states as NiMo alloys, along with some MoO_{3-x} phase. This arrangement highlights the development of a NiMo-MoO_{3-x} bifunctional group structure, emphasizing substantial synergy between the alloy and oxide constituents. An ICP-OES analysis (Table S1) showed an Ni : Mo atomic ratio of approximately 2.5 : 1 in the NiMo-MoO_{3-x}-HNT catalyst, suggesting that the exact chemical composition is $Ni_{2.5}Mo_{1-y}$-$yMoO_{3-x}$ ($0 < y < <1$).

Furthermore, XPS analysis was employed to examine the influence of reducing temperatures on the chemical states, chemical composition, and synergistic properties of the prepared catalysts (Figure S5). The catalysts prepared at 400°C showed oxide (Ni^{2+}, Mo^{4+}, and Mo^{6+}) and alloy (Ni^0 and Mo^0) peaks, indicative of the incomplete reduction of the precursor. The catalysts prepared at ≥600°C exhibited primarily alloy peaks with only a trace of oxide peaks. In addition, a significant negative shift was observed in the BE of Mo^0 because of the decrease in the MoO_{3-x} content and splitting of the Mo metal; thus, there may be less synergy between the alloy and oxide contents, as well as between Ni and Mo, compared with that of Ni-Mo-500. Based on the XPS analysis, the effective interaction between Ni, Mo, and MoO_{3-x} occurred when the catalyst was prepared at 500°C. Therefore, the chemical composition of the catalysts can be tuned by adjusting the reduction annealing temperature, which can affect the catalytic activities.

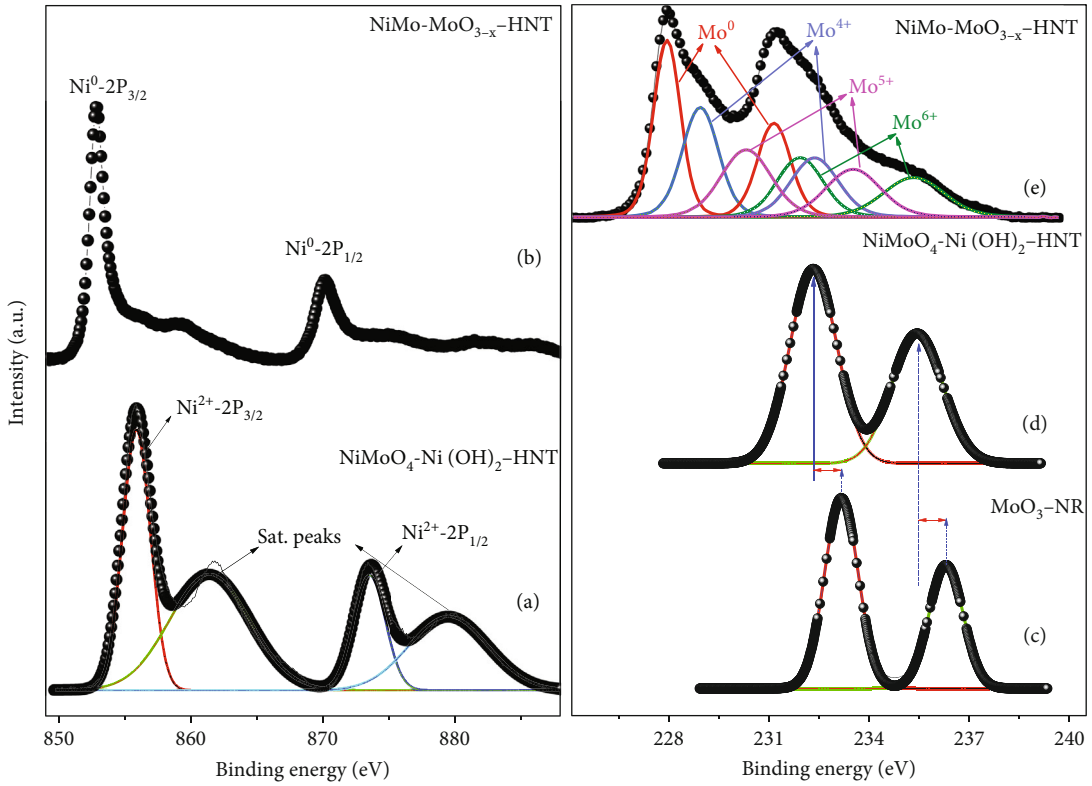

FIGURE 5: Ni-2*p* core-level XPS spectra of (a) $NiMoO_4$-$Ni(OH)_2$-HNT and (b) NiMo-MoO_{3-x}-HNT. Mo-3*d* core-level XPS spectra of (c) MoO_3-NR, (d) $NiMoO_4$-$Ni(OH)_2$-HNT, and (e) NiMo-MoO_{3-x}-HNT.

The chemical compositions of the prepared catalysts were assessed using Fourier-transform infrared spectroscopy, as shown in Figure S6. The prepared MoO_3-NR exhibited peaks at 545 (bending vibration of Mo_3-O), 875 (stretching vibration of Mo_2-O), and 997 cm^{-1} (asymmetric stretching of Mo=O), confirming the formation of MoO_3 [49]. The $NiMoO_4$-$Ni(OH)_2$-HNT exhibited peaks at 480 (Ni-O building group in $NiMoO_4$/$Ni(OH)_2$), 750 (symmetric stretching of Mo-O-Ni), 820 (asymmetric stretching of Mo_2-O), 864 (asymmetric stretching of Mo=O), and 925 cm^{-1} (symmetric stretching of Mo_2-O), evidencing the characteristic peaks of $NiMoO_4$ and $Ni(OH)_2$ and formation of the $NiMoO_4$-$Ni(OH)_2$-HNT. In addition, the IR peaks of MoO_3-NR almost vanished/shifted in the $NiMoO_4$-$Ni(OH)_2$-HNT, indicating the transition of MoO_3-NR to $NiMoO_4$, which is consistent with the XRD and XPS results. The Ni-Mo-400, which exhibited the characteristic peaks of its precursor, proved that the precursor was incompletely reduced in the NiMo alloy. However, the intensity of the oxide peaks in Ni-Mo-500 was lower than in Ni-Mo-400, indicating that Ni-Mo-500 contained a minimal amount of oxide content (733 cm^{-1} of Mo-O-Ni, 845 cm^{-1} of Mo_2-O, and 925 cm^{-1} of Mo = O), which enabled the development of the NiMo-MoO_{3-x}-HNT. In contrast, the NiMo alloy produced at ≥600°C showed no oxide peaks, suggesting the maximal transition of the precursor oxide into the alloy.

The N_2 adsorption–desorption measurements were performed to investigate the BET surface area and porosity of the $NiMoO_4$-$Ni(OH)_2$-HNT and Ni-Mo-500 (Figure S7). The isotherms can be classified as type IV patterns in the presence of H3-type hysteresis loops, indicating their porous structures. The $NiMoO_4$-$Ni(OH)_2$-HNT exhibited a high specific surface area and pore volume of 274.3 $m^2 g^{-1}$ and 0.46 $cm^3 g^{-1}$, respectively, due to the hierarchical HNT structure. After undergoing reduction heat treatment at 500°C, NiMo-MoO_{3-x}-HNT showed reduced values of 82.5 $m^2 g^{-1}$ and 0.25 $cm^3 g^{-1}$ due to the formation of the alloy resulting from the removal of oxygen during the thermal reduction process. As the reducing temperature was increased further, as shown in Figure S8, the surface area and pore volume of the NiMo alloys decreased to 26.4 $m^2 g^{-1}$ and 0.11 $cm^3 g^{-1}$, respectively, leading to the collapse and shrinkage of the HNT structure, as confirmed in Figure S3. Thus, the optimized NiMo-MoO_{3-x}-HNT electrocatalyst prepared at 500°C is a metal alloy-oxide bifunctional group with synergy between the alloy and oxide components. Furthermore, it has a porous hierarchical hollow nanotubular morphology with an optimal surface area, which are ideal features for an HER electrocatalyst.

5.2. Electrocatalytic Hydrogen Evolution Performance of NiMo-MoO_{3-x}-HNT. The electrocatalytic HER performances of the prepared catalysts and their precursors were assessed based on their polarization curves (I-V plots) at a sweep rate of 5 $mV s^{-1}$, as illustrated in Figure 6. As shown in Figure 6(a), the electrocatalytic HER activity of the catalysts

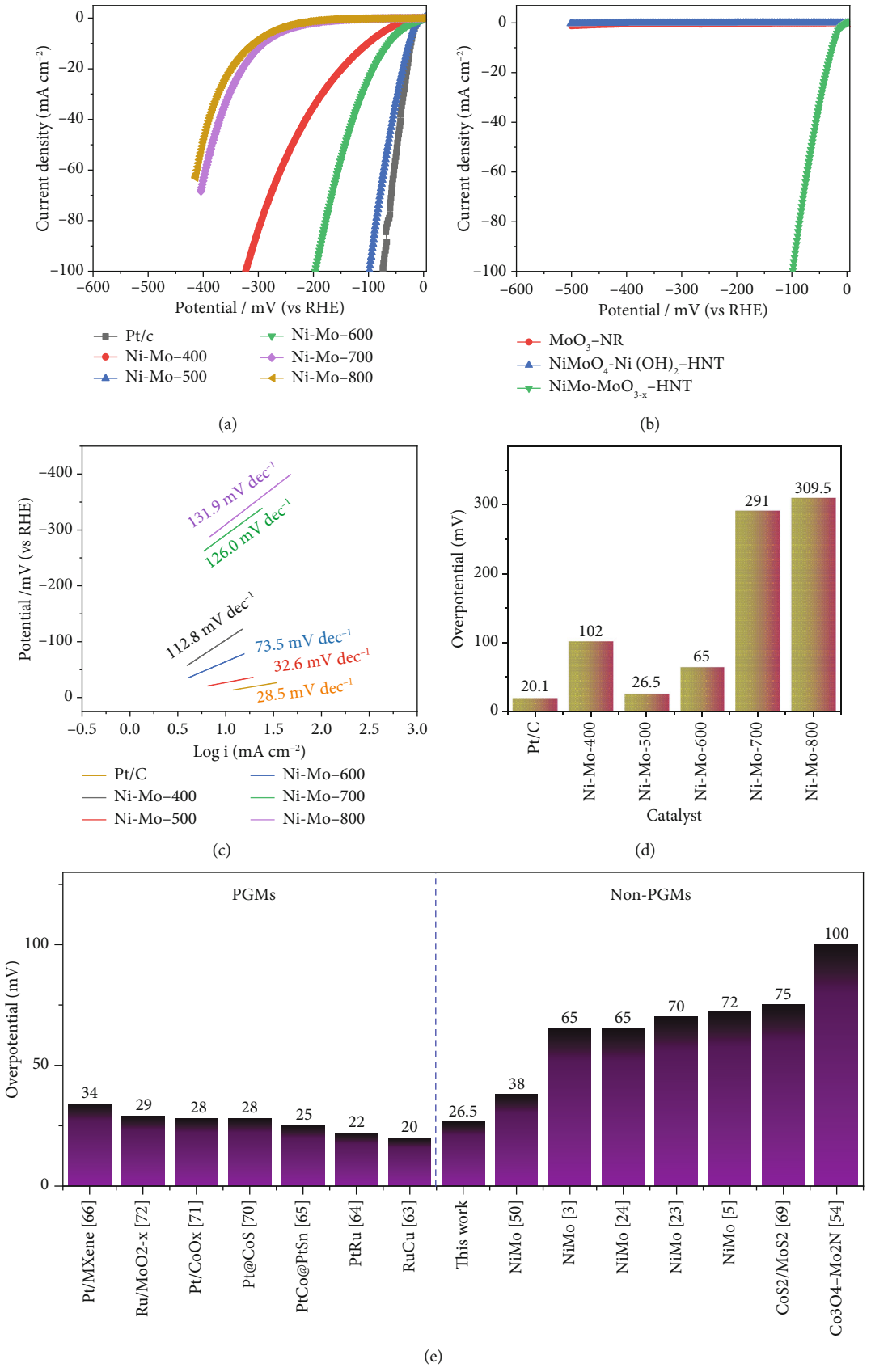

FIGURE 6: (a) LSV plots of Pt/C and catalysts prepared at different reduction annealing temperatures. (b) LSV plots of NiMo-MoO_{3-x}-HNT and its precursors. All LSV plots were measured at a 5 mV s^{-1} scan rate. (c) Tafel plots of prepared catalysts and Pt/C. (d) Overpotentials of prepared catalysts and Pt/C. (e) Comparison of NiMo-MoO_{3-x}-HNT overpotential with PGMs and non-PGMs based powder electrocatalysts.

followed the order Ni-Mo-800 < Ni-Mo-700 < Ni-Mo-400 < Ni-Mo-600 < Ni-Mo-500, whereas the precursors showed negligible performance (Figure 6(b)). The HER performance of the NiMo-MoO_{3-x}-HNT (Ni-Mo-500) was outstanding, requiring only an overpotential of 26.5 mV to generate a current density of 10 mA cm^{-2}, which was closer to that of Pt/C (20.1 mV).

To better understand the HER kinetics of the catalysts, Tafel curves were obtained from the corresponding LSV plots (Figure 6(a)), which are presented in Figure 6(c). Ni-Mo-500 had a significantly small Tafel slope of 32.6 mV dec^{-1}, lower than those of other prepared alloys and recently reported non-PGM-based powder electrocatalysts [3, 5, 23, 24, 50–61]. Moreover, its slope was comparable to that of the Pt/C (28.5 mV dec^{-1}) and state-of-the-art PGM-based electrocatalysts [62–66]. The low Tafel slope of Ni-Mo-500 indicated that the HER was accelerated in the alkaline medium, which involved fast kinetics. Typically, in an alkaline medium, hydrogen evolution occurs via two mechanisms: the Volmer–Heyrovsky (1 + 2) and Volmer–Tafel (1 + 3) mechanisms, expressed as follows:

$$H_2O + e^- \longrightarrow H^* + OH^- \quad (1)\,Volmer\ reaction$$

$$H^* + H_2O + e^- \longrightarrow H_2 + OH^- \quad (2)\,Heyrovsky\ reaction$$

$$2H^* \longrightarrow H_2 \quad (3)\,Tafel\ reaction$$

The low Tafel slope value of only 32.6 mV dec^{-1} for the Ni-Mo-500 catalyst indicated that the HER followed the faster Volmer–Tafel model, and the chemical desorption of hydrogen, i.e., the Tafel step, was the corresponding rate-determining step [65, 67, 68].

The performance of Ni-Mo-500 is notably superior to that of state-of-the-art NPGM-based powder electrocatalysts (Figure 6(e)) [3, 5, 23, 24, 50, 54, 69], which include MoNi microspheres (overpotential 72 mV; Tafel slope 36.6 mV dec^{-1}) [5], Mo-Ni-based hollow structure microspheres (overpotential 38 mV; Tafel slope 31.4 mV dec^{-1}) [56], and Co_3O_4–Mo_2N (overpotential 100 mV; Tafel slope 162.4 mV dec^{-1}) [54]. Furthermore, a comparison with PGM-based catalysts (Figure 6(e)) [63–66, 70–72], such as PtCo@PtSn (overpotential 25 mV; Tafel slope 24 mV dec^{-1}) [65] and Pt/MXene (overpotential 34 mV; Tafel slope 29.7 mV dec^{-1}) [66], further supports its comparable performance. The two factors responsible for the high HER activity of Ni-Mo-500 are as follows:

(1) Bifunctional properties of metal-metal oxide. Our recent DFT simulation study explained the bifunctional properties of NiMo alloy and MoO_{3-x} [73]. In NiMo alloy systems, electrons transfer from the electron-rich Ni to the electron-deficient Mo, resulting in Mo acting as a site that adsorbs H_2O molecules [74]. When MoO_{3-x} is introduced into the NiMo alloy, the adsorption-free energy of H_2O on the Mo center becomes more negative, indicating a preference for H_2O adsorption. This strong H_2O adsorption on the Mo center of NiMo-MoO_{3-x} lowers the energy barrier of O-H bond cleavage, further accelerating the H_2 production rate. After O-H dissociation, OH remains at the Mo center, while H shifts to the Ni center, leading to subsequent H_2 evolution. The Ni center is preferred for H_2 evolution over the Mo center due to the lower hydrogen adsorption energy. DFT analysis demonstrated that, compared to the NiMo alloy, the Ni center of NiMo-MoO_{3-x} exhibited an adsorption-free energy of H ∗ closer to zero, indicating facilitation of the HER reaction

(2) Morphological advantages. The porous hierarchical hollow nanotubular morphology of the NiMo-MoO_{3-x}-HNT provides a large catalytic surface area for the HER. The core 1D tubular structure facilitated rapid charge transport during electrolysis, and the porous hollow morphology sustained the accessibility of the electrolyte

To assess the intrinsic activity of NiMo-MoO_{3-x}-HNT, the turnover frequency (TOF) per active site of the catalyst in the HER process was determined, as outlined in the supporting information. The TOF of Ni-Mo-500 catalyst with a loading of 1.88 mg cm^{-2} is determined to be 0.1307 H_2 molecules s^{-1} at an overpotential of 100 mV, which is higher than those of reported HER catalysts, such as 0.1 mg cm^{-2} loaded Ni-Mo alloy (0.05 H_2 molecules s^{-1}), 1.6 mg cm^{-2} loaded NiMoFe alloy (0.05 H_2 molecules s^{-1}), and ~1.0 mg cm^{-2} loaded Ni_2P nanoparticles (0.012 H_2 molecules s^{-1}) [23, 75, 76]. Impedance analysis was utilized to examine the charge-transfer kinetics of the prepared catalysts. For a more comprehensive analysis, Nyquist plots were fitted with an equivalent circuit consisting of electrolyte resistance, charge transfer resistance, and constant phase element [77]. As illustrated in Figure S9, NiMo-MoO_{3-x}-HNT, characterized by the smallest semicircle, exhibited the lowest charge-transfer resistance among all the prepared catalysts, even comparable to Pt/C (Figure S9c). The electrochemical double layer capacitance (C_{dl}) of a catalyst is a significant characteristic for evaluating its electrochemical active surface area (ECSA and ECSAαC_{dl}) and intrinsic catalytic activity. Among all the prepared Ni-Mo alloys (Figure S10), the NiMo-MoO_{3-x}-HNT catalyst exhibited the maximum C_{dl} of 121 mF cm^{-2}, indicating that its greater ECSA contributed to its strong catalytic activity. The higher C_{dl} of the NiMo-MoO_{3-x}-HNT catalyst is attributed to its hierarchical nanotubular morphology with a high surface area and the optimal composition of its alloy and oxide particles.

5.3. Cycle Life Stability and Durability of NiMo-MoO_{3-x}-HNT. In addition to electrocatalytic activity, the stability of a catalyst is an important consideration when evaluating it for industrial hydrogen production. The stability of the NiMo-MoO_{3-x}-HNT (Ni-Mo-500) was investigated using CV measurements, as shown in Figure 7(a). After 50,000 cycles of operation, the NiMo-MoO_{3-x}-HNT almost retained current density and overpotential (changed from 26.5 mV to

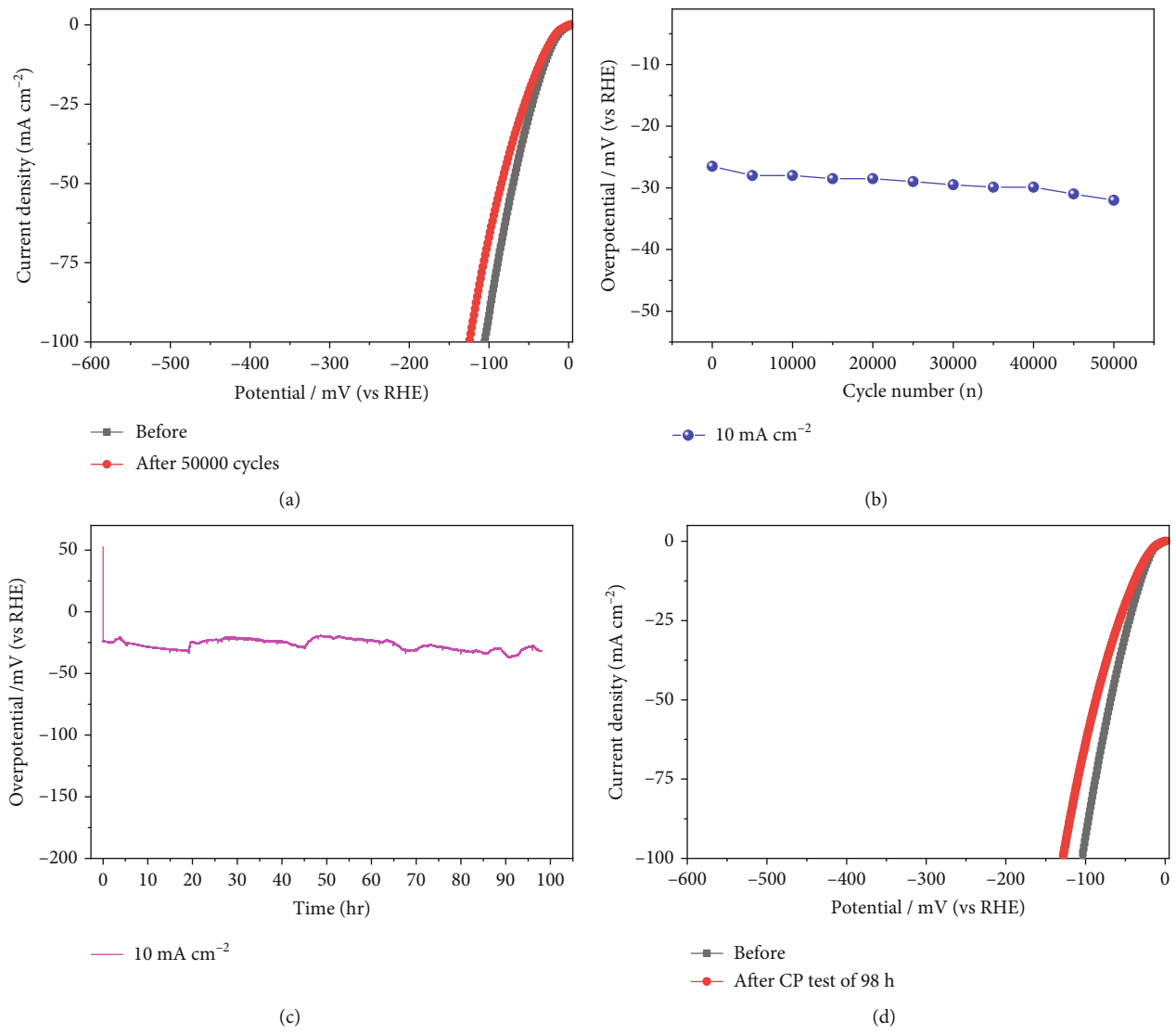

Figure 7: (a) LSV plots of NiMo-MoO_{3-x}-HNT before and after 50000 CV cycles, (b) variation of overpotential with cycle number at 10 mA cm^{-2} current density, (c) chronopotentiometric stability test of NiMo-MoO_{3-x}-HNT conducted at 10 mA cm^{-2} current density, and (d) LSV curves of NiMo-MoO_{3-x}-HNT before and after chronopotentiometric durability test.

32 mV, Figure 7(b)), demonstrating its outstanding stability. Furthermore, the durability of the NiMo-MoO_{3-x}-HNT was investigated using the CP method at 10 mA cm^{-2} for 98 h (Figure 7(c)). The NiMo-MoO_{3-x}-HNT showed excellent durability, exhibiting an almost unchanged overpotential (Figure 7(d)) after 98 h of hydrogen production. The morphological investigation of the NiMo-MoO_{3-x}-HNT after the cycle test indicated that its hierarchical hollow nanotubular structure was well preserved even after 50,000 cycles (Figure S11), which ensured its catalytic durability for the HER and its structural stability. In addition, the EDAX mapping analysis detected Ni, Mo, K, and O; the retention of Ni and Mo indicated the high chemical stability of the catalyst (Figure S12). The presence of K in the catalyst was due to the KOH electrolyte penetrating and getting trapped inside the core level of the catalyst during the cycle-life analysis.

The examination of chemical states following the cycle life test using XPS is presented in Figure S13. The deconvolution of Ni-2*p* XPS peaks in NiMo-MoO_{3-x}-HNT revealed the presence of Ni-H_{ad} (hydrogen adsorbed in Ni). This occurrence can be attributed to the role of Ni as a center for proton adsorption (H ∗), contributing to H_2 formation [78, 79]. The observation of the Ni^{2+} state suggests the formation of nickel oxide due to Ni^0 interaction with the KOH electrolyte. The deconvoluted Mo-3*d* peaks indicate a transformation from the Mo^0 to the Mo^{6+}. Mo plays a vital role in accelerating the adsorption of water molecules and the dissociation of H-OH. As a result, during the repeated cycling process, the Mo surface undergoes a transition to a higher oxidation state, which is reflected in the XPS. Notably, the BE of Ni^0-$2p_{3/2}$ and Mo^{6+}-$3d_{5/2}$ exhibit little change even after cycling, indicating that the catalyst retains its metal-metal

oxide synergy effect. As confirmed by EDAX, the presence of K in the catalyst was also observed in XPS after the cycle life test, indicating that the KOH electrolyte had penetrated inside the catalyst (Figure S13b). Overall, the NiMo-MoO_{3-x}-HNT demonstrates good cycle stability and high catalytic activity due to its structural robustness and bifunctional effect. This high catalytic efficiency and long-term stability hold promise for the potential commercialization of cost-effective NiMo-MoO_{3-x}-HNT in the near future.

6. Conclusions

This study demonstrates a novel approach to synthesizing a highly efficient electrocatalyst for the hydrogen evolution reaction based on a NiMo-MoO_{3-x} bifunctional hollow nanotube using MoO_3-NR as a 1D template and Mo source. The generation of hierarchical nanotubes was regulated by the hydrothermal reaction time, resulting in the formation of Kirkendall voids at an optimal reaction time of 5 h. The NiMo-MoO_{3-x}-HNT catalyst prepared at an annealing temperature of 500°C emerged as the optimal catalyst, combining a bifunctional metal alloy-oxide structure with a hierarchical hollow nanotubular morphology. This resulted in a favorable surface area and porosity, which are desirable attributes for efficient HER electrocatalysis. The NiMo-MoO_{3-x} catalyst demonstrated efficient HER performance with a low overpotential of 26.5 mV and minimal Tafel slope of 32.6 mV dec^{-1}. Further analysis through impedance measurements validated the efficient charge-transfer kinetics and a substantial electrochemically active surface area. Importantly, the NiMo-MoO_{3-x} catalyst displayed exceptional stability and durability, maintaining a nearly unaltered performance over 50,000 cycles and 98 h of continuous operation. These findings establish the NiMo-MoO_{3-x} catalyst as a viable and prospective alternative to electrocatalysts containing precious metals, particularly for industrial applications.

Data Availability

The data that support the findings of this study are available from the first author upon reasonable request.

Conflicts of Interest

The authors declare no interest conflict. They have no known competing financial interests or personal relationships that could have appeared to influence the work reported in this paper.

Acknowledgments

This research was supported by the Basic Science Research Program through the National Research Foundation of Korea (NRF) funded by the Ministry of Education (NRF-2019R1A6A1A11055660 and NRF-2022R1I1A1A01069960) and Strategic Networking & Development Program funded by the Ministry of Science and ICT through the National Research Foundation of Korea (RS-2023-00268523).

Supplementary Materials

Electronic supporting information covers data of morphology analysis of MoO3 and nickel acetate dispersion in water/ethanol. EDAX mapping images of NiMo-MoO_{3-x}-HNT. FE-SEM images of the Ni-Mo alloys prepared at different reduction temperatures. ICP and EDAX analyses of Ni-Mo alloys prepared at different reduction temperatures. XRD patterns of $NiMoO_4$-$Ni(OH)_2$-HNT prepared at 90°C for different reaction time intervals. Ni-2*p* and Mo-3*d* core-level XPS spectra of Ni-Mo alloys prepared at different reduction temperatures. FT-IR spectrum of MoO_3-NR, $NiMoO_4$-$Ni(OH)_2$-HNT, and Ni-Mo alloys prepared at different reduction temperatures. N_2 adsorption and desorption isotherms and pore size distribution curves of $NiMoO_4$-$Ni(OH)_2$-HNT and NiMo-MoO_{3-x}-HNT. Impedance analysis of NiMo-MoO_{3-x}-HNT and its precursors, Ni-Mo alloys prepared at different reduction annealing temperatures, and NiMo-MoO_{3-x}-HNT and Pt/C. CV curves of Ni-Mo-400, Ni-Mo-500, Ni-Mo-600, Ni-Mo-700, and Ni-Mo-800 recorded in 1 M KOH solution at various sweep rates from 20 to 50 mV s^{-1}. C_{dl} value comparison of Ni-Mo-400, Ni-Mo-500, Ni-Mo-600, Ni-Mo-700, and Ni-Mo-800. FE-SEM images of NiMo-MoO_{3-x}-HNT before and after cycle life analysis. EDAX mapping analysis of NiMo-MoO_{3-x}-HNT after cycle life analysis. XPS analysis of NiMo-MoO_{3-x}-HNT after cycle life analysis. *(Supplementary Materials)*

References

[1] Q. Lu, Y. Yu, Q. Ma, B. Chen, and H. Zhang, "2D transition-metal-dichalcogenide-nanosheet-based composites for photocatalytic and electrocatalytic hydrogen evolution reactions," *Advanced Materials*, vol. 28, no. 10, pp. 1917–1933, 2016.

[2] S. Xu, X. Yu, L. Luo et al., "Multiscale manipulating induced flexible heterogeneous V-NiFe2O4@Ni2P electrocatalyst for efficient and durable oxygen evolution reaction," *Nano Research*, vol. 15, no. 6, pp. 4942–4949, 2022.

[3] D. D. Rodene, E. H. Eladgham, R. B. Gupta, I. U. Arachchige, and V. Tallapally, "Crystal structure and composition-dependent electrocatalytic activity of Ni–Mo nanoalloys for water splitting to produce hydrogen," *ACS Applied Energy Materials*, vol. 2, no. 10, pp. 7112–7120, 2019.

[4] S. Han, Q. Yun, S. Tu, L. Zhu, W. Cao, and Q. Lu, "Metallic ruthenium-based nanomaterials for electrocatalytic and photocatalytic hydrogen evolution," *Journal of Materials Chemistry A*, vol. 7, no. 43, pp. 24691–24714, 2019.

[5] L. Yang, L. Zeng, H. H. Liu et al., "Hierarchical microsphere of MoNi porous nanosheets as electrocatalyst and cocatalyst for hydrogen evolution reaction," *Applied Catalysis B: Environmental*, vol. 249, pp. 98–105, 2019.

[6] L. Li, J. Meng, X. Bao et al., "Direct-ink-write 3D printing of programmable micro-supercapacitors from MXene-regulating conducting polymer inks," *Advanced Energy Materials*, vol. 13, no. 9, pp. 1–12, 2023.

[7] R. Jin, J. Huang, G. Chen et al., "Water-sprouted, plasma-enhanced Ni-Co phospho-nitride nanosheets boost electrocatalytic hydrogen and oxygen evolution," *Chemical Engineering Journal*, vol. 402, article 126257, 2020.

[8] J. Chen, Y. Yang, J. Su, P. Jiang, G. Xia, and Q. Chen, "Enhanced activity for hydrogen evolution reaction over CoFe catalysts by alloying with small amount of Pt," *ACS Applied Materials & Interfaces*, vol. 9, no. 4, pp. 3596–3601, 2017.

[9] X. Li, X. Hao, A. Abudula, and G. Guan, "Nanostructured catalysts for electrochemical water splitting: current state and prospects," *Journal of Materials Chemistry A*, vol. 4, no. 31, pp. 11973–12000, 2016.

[10] N. K. Chaudhari, H. Jin, B. Kim, and K. Lee, "Nanostructured materials on 3D nickel foam as electrocatalysts for water splitting," *Nanoscale*, vol. 9, no. 34, pp. 12231–12247, 2017.

[11] J. R. McKone, E. L. Warren, M. J. Bierman et al., "Evaluation of Pt, Ni, and Ni-Mo electrocatalysts for hydrogen evolution on crystalline Si electrodes," *Energy and Environmental Science*, vol. 4, no. 9, pp. 3573–3583, 2011.

[12] W. F. Chen, K. Sasaki, C. Ma et al., "Hydrogen-evolution catalysts based on non-noble metal nickel-molybdenum nitride nanosheets," *Angewandte Chemie-International Edition*, vol. 51, no. 25, pp. 6131–6135, 2012.

[13] Q. Zhang, P. Li, D. Zhou, Z. Chang, Y. Kuang, and X. Sun, "Superaerophobic ultrathin Ni–Mo alloy nanosheet array from in situ topotactic reduction for hydrogen evolution reaction," *Small*, vol. 13, no. 41, pp. 1–7, 2017.

[14] Z. Chen, X. Duan, W. Wei, S. Wang, and B. J. Ni, "Recent advances in transition metal-based electrocatalysts for alkaline hydrogen evolution," *Journal of Materials Chemistry A*, vol. 7, no. 25, pp. 14971–15005, 2019.

[15] H. Zhou, Y. Wang, R. He et al., "One-step synthesis of self-supported porous NiSe2/Ni hybrid foam: an efficient 3D electrode for hydrogen evolution reaction," *Nano Energy*, vol. 20, pp. 29–36, 2016.

[16] X. Wang, B. Zheng, B. Yu et al., "In situsynthesis of hierarchical MoSe2–CoSe2nanotubes as an efficient electrocatalyst for the hydrogen evolution reaction in both acidic and alkaline media," *Journal of Materials Chemistry A*, vol. 6, no. 17, pp. 7842–7850, 2018.

[17] X. X. X. Zhang, J. Guo, X. X. X. Zhang, Y. Sun, and L. Tang, "Self-template synthesis of hierarchical CoMoS3nanotubes constructed of ultrathin nanosheets for robust water electrolysis," *Journal of Materials Chemistry A*, vol. 5, no. 22, pp. 11309–11315, 2017.

[18] S. L. Zhang, X. F. Lu, Z. P. Wu, D. Luan, and X. W. Lou, "Engineering platinum–cobalt nano-alloys in porous nitrogen-doped carbon nanotubes for highly efficient electrocatalytic hydrogen evolution," *Angewandte Chemie-International Edition*, vol. 60, no. 35, pp. 19068–19073, 2021.

[19] T. Feng, G. Yu, S. Tao et al., "A highly efficient overall water splitting ruthenium-cobalt alloy electrocatalyst across a wide pH rangeviaelectronic coupling with carbon dots," *Journal of Materials Chemistry A*, vol. 8, no. 19, pp. 9638–9645, 2020.

[20] G. Liu, W. Zhou, B. Chen et al., "Synthesis of RuNi alloy nanostructures composed of multilayered nanosheets for highly efficient electrocatalytic hydrogen evolution," *Nano Energy*, vol. 66, p. 104173, 2019.

[21] H. Jin, C. Guo, X. Liu et al., "Emerging two-dimensional nanomaterials for electrocatalysis," *Chemical Reviews*, vol. 118, no. 13, pp. 6337–6408, 2018.

[22] M. Xia, T. Lei, N. Lv, and N. Li, "Synthesis and electrocatalytic hydrogen evolution performance of Ni-Mo-Cu alloy coating electrode," *International Journal of Hydrogen Energy*, vol. 39, no. 10, pp. 4794–4802, 2014.

[23] J. R. McKone, B. F. Sadtler, C. A. Werlang, N. S. Lewis, and H. B. Gray, "Ni-Mo nanopowders for efficient electrochemical hydrogen evolution," *ACS Catalysis*, vol. 3, no. 2, pp. 166–169, 2013.

[24] T. Zhang, X. Liu, X. Cui, M. Chen, S. Liu, and B. Geng, "Colloidal synthesis of Mo–Ni alloy nanoparticles as bifunctional electrocatalysts for efficient overall water splitting," *Advanced Materials Interfaces*, vol. 5, no. 13, pp. 1–6, 2018.

[25] V. R. Stamenkovic, D. Strmcnik, P. P. Lopes, and N. M. Markovic, "Energy and fuels from electrochemical interfaces," *Nature Materials*, vol. 16, pp. 57–69, 2017.

[26] H. J. W. Li, K. Liu, J. Fu et al., "Paired Ru–O–Mo ensemble for efficient and stable alkaline hydrogen evolution reaction," *Nano Energy*, vol. 82, article 105767, 2021.

[27] X. Lu, M. Cai, Z. Zou, J. Huang, and C. Xu, "A novel MoNi@-Ni(OH)2 heterostructure with Pt-like and stable electrocatalytic activity for the hydrogen evolution reaction," *Chemical Communications*, vol. 56, no. 11, pp. 1729–1732, 2020.

[28] N. Danilovic, R. Subbaraman, D. Strmcnik et al., "Enhancing the alkaline hydrogen evolution reaction activity through the bifunctionality of Ni(OH) 2/metal catalysts," *Angewandte Chemie*, vol. 124, no. 50, pp. 12663–12666, 2012.

[29] J. Li, B. Li, H. Huang et al., "Polyvinylpyrrolidone gel based Pt/Ni(OH)2heterostructures with redistributing charges for enhanced alkaline hydrogen evolution reaction," *Journal of Materials Chemistry A*, vol. 9, no. 47, pp. 27061–27071, 2021.

[30] Z. Liu, K. Wang, Y. Li, and Y. Cao, "Interface-induced electron transfer in sandwich-like hierarchical hollow CoP@NC hybrid for boosted hydrogen evolution reaction in alkaline electrolyte," *Journal of Alloys and Compounds*, vol. 956, p. 170315, 2023.

[31] L. Jia, C. Li, Y. Zhao et al., "Interfacial engineering of Mo2C–Mo3C2heteronanowires for high performance hydrogen evolution reactions," *Nanoscale*, vol. 11, no. 48, pp. 23318–23329, 2019.

[32] D. Mandal, P. Routh, and A. K. Nandi, "Quantum-dot-mediated controlled synthesis of dual oxides of molybdenum from MoS_2: quantification of supercapacitor efficacy," *Chemistry-An Asian Journal*, vol. 13, pp. 3871–3884, 2018.

[33] D. Mandal, J. Y. Jeong, B. S. Singu, S. Lee, W. J. Mun, and H. Kim, "Flexible all solid-state niobium nitride//activated carbon lithium-ion hybrid capacitor with high volumetric power and energy densities," *Journal of Energy Storage*, vol. 48, article 104031, 2022.

[34] S. Zhuo, Y. Xu, W. Zhao, J. Zhang, and B. Zhang, "Hierarchical nanosheet-based MoS2 nanotubes fabricated by an anion-exchange reaction of MoO3-amine hybrid nanowires," *Angewandte Chemie-International Edition*, vol. 52, no. 33, pp. 8602–8606, 2013.

[35] C. Gu, W. Guan, Y. Cui, Y. Chen, L. Gao, and J. Huang, "Preparation of three-dimensional nanosheet-based molybdenum disulfide nanotubes as anode materials for lithium storage," *Journal of Materials Chemistry A*, vol. 4, no. 43, pp. 17000–17008, 2016.

[36] Z. Wu, Z. Wang, and F. Geng, "Radially aligned hierarchical nickel/nickel-iron (oxy)hydroxide nanotubes for efficient electrocatalytic water splitting," *ACS Applied Materials and Interfaces*, vol. 10, no. 10, pp. 8585–8593, 2018.

[37] K. Zhang, C. Li, Y. Zhao, X. Yu, and Y. Chen, "Porous one-dimensional Mo2C-amorphous carbon composites: high-efficient and durable electrocatalysts for hydrogen generation,"

Physical Chemistry Chemical Physics, vol. 17, no. 25, pp. 16609–16614, 2015.

[38] M. Yang, C. H. Zhang, N. W. Li, D. Luan, L. Yu, and X. W. Lou, "Design and synthesis of hollow nanostructures for electrochemical water splitting," *Advanced Science*, vol. 9, no. 9, article e2105135, 2022.

[39] J. Li and G. Zheng, "One-dimensional earth-abundant nanomaterials for water-splitting electrocatalysts," *Advanced Science*, vol. 4, no. 3, 2017.

[40] M. Fang, G. Dong, R. Wei, and J. C. Ho, "Hierarchical nanostructures: design for sustainable water splitting," *Advanced Energy Materials*, vol. 7, no. 23, pp. 1–25, 2017.

[41] J. S. Chen, Y. L. Cheah, S. Madhavi, and X. W. Lou, "Fast synthesis of α-MoO3nanorods with controlled aspect ratios and their enhanced lithium storage capabilities," *Journal of Physical Chemistry C*, vol. 114, no. 18, pp. 8675–8678, 2010.

[42] X. W. Lou and H. C. Zeng, "Hydrothermal synthesis of α-MoO3nanorods via acidification of ammonium heptamolybdate tetrahydrate," *Chemistry of Materials*, vol. 14, no. 11, pp. 4781–4789, 2002.

[43] N. Parveen and M. H. Cho, "Self-assembled 3D flower-like nickel hydroxide nanostructures and their supercapacitor applications," *Scientific Reports*, vol. 6, no. 1, article 27318, 2016.

[44] H. Tianou, W. Wang, X. Yang et al., "Inflating hollow nanocrystals through a repeated Kirkendall cavitation process," *Nature Communications*, vol. 8, no. 1, p. 1261, 2017.

[45] M. Schalenbach, F. D. Speck, M. Ledendecker et al., "Nickel-molybdenum alloy catalysts for the hydrogen evolution reaction: activity and stability revised," *Electrochimica Acta*, vol. 259, pp. 1154–1161, 2018.

[46] V. Sudheendra Budhiraju, A. Sharma, and S. Sivakumar, "Structurally stable mesoporous hierarchical NiMoO4hollow nanofibers for asymmetric supercapacitors with enhanced capacity and improved cycling stability," *Chem Electro Chem*, vol. 4, no. 12, pp. 3331–3339, 2017.

[47] A. P. Grosvenor, M. C. Biesinger, R. S. C. Smart, and N. S. McIntyre, "New interpretations of XPS spectra of nickel metal and oxides," *Surface Science*, vol. 600, no. 9, pp. 1771–1779, 2006.

[48] D. Huang, S. Li, Y. Luo, L. Liao, J. Ye, and H. Chen, "Self-templated construction of 1D NiMo nanowiresviaa Li electrochemical tuning method for the hydrogen evolution reaction," *Nanoscale*, vol. 11, no. 41, pp. 19429–19436, 2019.

[49] L. Fang, Y. Shu, A. Wang, and T. Zhang, "Green synthesis and characterization of anisotropic uniform single-crystal α-MoO3nanostructures," *Journal of Physical Chemistry C*, vol. 111, no. 6, pp. 2401–2408, 2007.

[50] Y. Zhou, M. Luo, W. Zhang et al., "Topological formation of a Mo-Ni-based hollow structure as a highly efficient electrocatalyst for the hydrogen evolution reaction in alkaline solutions," *ACS Applied Materials & Interfaces*, vol. 11, no. 24, pp. 21998–22004, 2019.

[51] F. Yang, J. Hong, J. Hao et al., "Ultrathin few-layer gep nanosheets via lithiation-assisted chemical exfoliation and their application in sodium storage," *Advanced Energy Materials*, vol. 10, no. 14, article 1903826, 2020.

[52] H. Cheng, Y. Diao, Q. Liu et al., "Di-nuclear metal synergistic catalysis: Ni2Mo6S6O2/MoS2 two-dimensional nanosheets for hydrogen evolution reaction," *Chemical Engineering Journal*, vol. 428, article 131084, 2022.

[53] H. Liu, X. Qian, Y. Niu, M. Chen, C. Xu, and K. Y. Wong, "Hierarchical Ni-MoSex@CoSe2 core-shell nanosphere as highly active bifunctional catalyst for efficient dye-sensitized solar cell and alkaline hydrogen evolution," *Chemical Engineering Journal*, vol. 383, article 123129, 2020.

[54] T. Wang, P. Wang, W. Zang et al., "Nanoframes of Co3O4–Mo2N heterointerfaces enable high-performance bifunctionality toward both electrocatalytic HER and OER," *Advanced Functional Materials*, vol. 32, no. 7, article 2107382, 2022.

[55] J. Wang, S. Xin, Y. Xiao et al., "Manipulating the water dissociation electrocatalytic sites of bimetallic nickel-based alloys for highly efficient alkaline hydrogen evolution," *Angewandte Chemie International Edition*, vol. 61, no. 30, article e202202518, 2022.

[56] Q. Q. Pan, C. Y. Xu, X. Li et al., "Porous Ni-Mo bimetallic hybrid electrocatalyst by intermolecular forces in precursors for enhanced hydrogen generation," *Chemical Engineering Journal*, vol. 405, article 126962, 2021.

[57] J. Bao, Y. Zhou, Y. Zhang et al., "Engineering water splitting sites in three-dimensional flower-like co-Ni-P/MoS2heterostructural hybrid spheres for accelerating electrocatalytic oxygen and hydrogen evolution," *Journal of Materials Chemistry A*, vol. 8, no. 42, pp. 22181–22190, 2020.

[58] M. Kim, M. A. R. Anjum, M. Choi et al., "Covalent 0D–2D heterostructuring of Co9S8–MoS2for enhanced hydrogen evolution in all pH electrolytes," *Advanced Functional Materials*, vol. 30, no. 40, pp. 1–11, 2020.

[59] L. Diao, B. Zhang, Q. Sun et al., "An in-plane Co9S8@MoS2heterostructure for the hydrogen evolution reaction in alkaline media," *Nanoscale*, vol. 11, no. 44, pp. 21479–21486, 2019.

[60] J. Li, X. Gu, J. Chang et al., "Molybdenum oxide-iron, cobalt, copper alloy hybrid as efficient bifunctional catalyst for alkali water electrolysis," *Journal of Colloid and Interface Science*, vol. 606, Part 2, pp. 1662–1672, 2022.

[61] L. Chen, Z. Deng, Z. Chen, and X. Wang, "Building Ni9S8/MoS2nanosheets decorated NiMoO4nanorods heterostructure for enhanced water splitting," *Advanced Materials Interfaces*, vol. 8, no. 21, pp. 1–9, 2021.

[62] L. Li, G. Zhang, B. Wang, T. Yang, and S. Yang, "Electrochemical formation of PtRu bimetallic nanoparticles for highly efficient and pH-universal hydrogen evolution reaction," *Journal of Materials Chemistry*, vol. 8, no. 4, pp. 2090–2098, 2020.

[63] Q. Yao, B. Huang, N. Zhang, M. Sun, Q. Shao, and X. Huang, "Channel-rich RuCu nanosheets for pH-universal overall water splitting electrocatalysis," *Angewandte Chemie-International Edition*, vol. 58, no. 39, pp. 13983–13988, 2019.

[64] Y. Li, W. Pei, J. He et al., "Hybrids of PtRu nanoclusters and black phosphorus nanosheets for highly efficient alkaline hydrogen evolution reaction," *ACS Catalysis*, vol. 9, no. 12, pp. 10870–10875, 2019.

[65] J. Chen, G. Qian, H. Zhang et al., "PtCo@PtSn heterojunction with high stability/activity for pH-universal H2evolution," *Advanced Functional Materials*, vol. 32, no. 5, article 2107597, 2022.

[66] Y. Wu, W. Wei, R. Yu et al., "Anchoring sub-nanometer Pt clusters on crumpled paper-like MXene enables high hydrogen evolution mass activity," *Advanced Functional Materials*, vol. 32, no. 17, 2022.

[67] L. Zhang, Y. Jia, X. Yan, and X. Yao, "Activity origins in nanocarbons for the electrocatalytic hydrogen evolution reaction," *Small*, vol. 14, no. 26, article e1800235, 2018.

[68] Z. Zhuang, J. Huang, Y. Li, L. Zhou, and L. Mai, "The holy grail in platinum-free electrocatalytic hydrogen evolution: molybdenum-based catalysts and recent advances," *Chem Electro Chem*, vol. 6, no. 14, pp. 3570–3589, 2019.

[69] P. Liu, J. Yan, J. Mao, J. Li, D. Liang, and W. Song, "In-plane intergrowth CoS2/MoS2nanosheets: binary metal-organic framework evolution and efficient alkaline HER electrocatalysis," *Journal of Materials Chemistry A*, vol. 8, no. 22, pp. 11435–11441, 2020.

[70] A. Mosallanezhad, C. Wei, P. Ahmadian Koudakan et al., "Interfacial synergies between single-atomic Pt and CoS for enhancing hydrogen evolution reaction catalysis," *Applied Catalysis B: Environmental*, vol. 315, article 121534, 2022.

[71] Y. Wang, B. Zhu, B. Cheng, W. Macyk, P. Kuang, and J. Yu, "Hollow carbon sphere-supported Pt/CoOx hybrid with excellent hydrogen evolution activity and stability in acidic environment," *Applied Catalysis B: Environmental*, vol. 314, 2022.

[72] C. Li, H. Jang, M. G. Kim, L. Hou, X. Liu, and J. Cho, "Ru-incorporated oxygen-vacancy-enriched MoO2 electrocatalysts for hydrogen evolution reaction," *Applied Catalysis B: Environmental*, vol. 307, 2022.

[73] B. S. Singu, R. K. Chitumalla, D. Mandal et al., "Development of metal-organic framework-derived NiMo-MoO3−x porous nanorod for efficient electrocatalytic hydrogen evolution reactions," *Applied Catalysis B: Environmental*, vol. 328, 2023.

[74] J.-Y. Y. Zhang, T. He, M. Wang et al., "Energy-saving hydrogen production coupling urea oxidation over a bifunctional nickel-molybdenum nanotube array," *Nano Energy*, vol. 60, pp. 894–902, 2019.

[75] E. J. Popczun, J. R. McKone, C. G. Read et al., "Nanostructured nickel phosphide as an electrocatalyst for the hydrogen evolution reaction," *Journal of the American Chemical Society*, vol. 135, no. 25, pp. 9267–9270, 2013.

[76] F. Qin, Z. Zhao, M. K. Alam et al., "Trimetallic NiFeMo for overall electrochemical water splitting with a low cell voltage," *ACS Energy Letters*, vol. 3, no. 3, pp. 546–554, 2018.

[77] B. Zhong, S. Wan, P. Kuang, B. Cheng, L. Yu, and J. Yu, "Crystalline/amorphous Ni/NixSy supported on hierarchical porous nickel foam for high-current-density hydrogen evolution," *Applied Catalysis B: Environmental*, vol. 340, article 123195, 2024.

[78] J. Tang, S. Yamamoto, T. Koitaya et al., "Hydrogen adsorption and absorption on a Pd-Ag alloy surface studied using in-situ X-ray photoelectron spectroscopy under ultrahigh vacuum and ambient pressure," *Applied Surface Science*, vol. 463, pp. 1161–1167, 2019.

[79] S. J. Kerber, J. J. Bruckner, K. Wozniak, S. Seal, S. Hardcastle, and T. L. Barr, "The nature of hydrogen in x-ray photoelectron spectroscopy: general patterns from hydroxides to hydrogen bonding," *Journal of Vacuum Science & Technology A: Vacuum, Surfaces, and Films*, vol. 14, pp. 1314–1320, 1996.